Polymer 103 (2016) 315–327

Contents lists available at ScienceDirect

Polymer

journal homepage: www.elsevier.com/locate/polymer

Lowly loaded carbon nanotubes induced high electrical conductivity and giant magnetoresistance in ethylene/1-octene copolymers

Xingru Yan [a], Junwei Gu [b, *, 1], Guoqiang Zheng [c], Jiang Guo [a], Alexandra Maria Galaska [a], Jingfang Yu [d], Mojammel Alam Khan [e], Luyi Sun [d], David P. Young [e], Qiuyu Zhang [b], Suying Wei [f, **], Zhanhu Guo [a, ***]

[a] Integrated Composites Laboratory (ICL), Department of Chemical & Biomolecular Engineering, University of Tennessee, Knoxville, TN 37996, USA
[b] Department of Applied Chemistry, School of Science, Northwestern Polytechnical University, Xi'an, Shaan Xi, 710072, PR China
[c] College of Materials Science and Engineering, The Key Laboratory of Material Processing and Mold of Ministry of Education, Zhengzhou University, Zhengzhou, 450001, PR China
[d] Department of Chemical & Biomolecular Engineering and Polymer Program, Institute of Materials Science, University of Connecticut, Storrs, CT 06269, USA
[e] Department of Physics and Astronomy, Louisiana State University, Baton Rouge, LA 70803, USA
[f] Department of Chemistry and Biochemistry, Lamar University, Beaumont, TX 77710, USA

ARTICLE INFO

Article history:
Received 6 August 2016
Received in revised form
7 September 2016
Accepted 17 September 2016
Available online 19 September 2016

Keywords:
Giant magnetoresistance
Electrical conductivity
Surface gelation

ABSTRACT

High electrical conductivity in ethylene/1-octene copolymers (EOCs) was achieved by sticking CNTs onto the gelated EOCs pellet surface and the subsequent hot pressing. The electrical conductivity (σ) was observed to be dependent on the pressing temperature and the CNT loading. Variable range hopping (VRH) mechanistic study revealed a 3-d electron transport mechanism. Both unique positive and negative magnetoresistance (MR) phenomena were observed in these polymer nanocomposites (PNCs) and theoretically analyzed by two different models (wave-function shrinkage model for positive GMR vs. forward interference model for negative GMR). Other properties were tested and analyzed as well. Neat EOCs and their nanocomposites exhibited both Newtonian and shear thinning behaviors under melting state. Less internal chain-chain friction heat was generated than that of neat EOCs after applying the same oscillation frequencies. The increased thermal stability of EOC nanocomposites was observed with increasing the CNTs loading. An increased thermal conductivity (λ) was observed arising from the formed CNTs network.

1. Introduction

Polymer nanocomposites (PNCs) attract increasing interests and demonstrate strikingly favorable performances arising from unique physicochemical properties including economical processability and low density of polymers, and functional merits of nanofillers including excellent mechanical strength and tunable magnetic, electric, optical and dielectric properties [1–4]. Among nanocomposites, the conductive or semiconductive PNCs have captured growing interests arising from the introduced unique properties and potential usages including energy storing units [5–7], sensing devices [8–10], kinesiology [11–13], fire retardants [14–16], microwave absorbers [17–19], and aerospace vehicles [20]. Ordinarily, conductive PNCs can be made by using conductive nanofillers into insulative polymer. Among these reported conducting nanofillers, carbon nanotubes (CNTs) are highly flexible [21,22], light-weight [23], and posses large aspect ratio (typically ca. 300–1000) [24], much higher tensile modulus (640 GPa–1 TPa for single-walled CNTs (SWCNTs)) [25,26], and outstanding electrical and thermal conductivity. Since the first report by Iijima in 1991 [27], and the first report of using CNTs as fillers by Ajayan in 1994 [5], CNTs have substituted or complemented conventional nanofillers for preparing multifunctional PNCs [28,29]. The structural parameters can influence the properties of the CNTs such as the electronic properties with the existing either metallic or semiconducting and affect their applications. For example, CNTs can even serve as flame

* Corresponding author.
** Corresponding author.
*** Corresponding author.
E-mail addresses: gjw@nwpu.edu.cn (J. Gu), suying.wei@lamar.edu (S. Wei), zguo10@utk.edu (Z. Guo).
[1] The author Junwei Gu contributed equally to this work and should be considered as co-first authors.

http://dx.doi.org/10.1016/j.polymer.2016.09.056
0032-3861/

retardant. The interconnecting MWCNTs significantly enhanced the thermal stability and reduced the heat release rate of polypropylene (PP) [30]. However, the surface inertness and large aspect ratio challenge their dispersion; therefore, a high loading was needed to form a conductive network [31]. For example, no percolation behavior was observed in the in-situ polymerized PP PNCs even at ~3.5 wt% CNTs loading [32]. To enhance the conductivity, aligned CNTs were explored with a narrow diameter distribution and a given length by varying the production parameters [33]. Furthermore, different functional groups have been introduced to make them interracially compatible with polymer [34]. For instance, Barrau et al. [35] treated MWCNTs with palmitic acid and the resulted epoxy PNCs showed enhanced electrical conductivity (σ) with improved dispersion of CNTs. However, these treatments could decrease the σ of pure CNTs with damaged crystalline structure [36] and changed interfacial adhesion [37]. For example, Gojny et al. [38] reported a higher percolation threshold in the amino-functionalized CNTs than that in the pristine CNTs.

Block copolymers are produced by linking two or more chemically distinct polymer blocks [39]. In the solid and rubbery states, copolymers have been used as thermoplastic elastomers offering combined characteristics of rubber and plastic [40]. Copolymers of ethylene with α-olefins are now commercially available for wide applications [41]. Ethylene/1-octene copolymers (EOCs) are the most important copolymers and can be used as good toughening modifier for PP [42,43], polycarbonate (PC) [44] and high density polyethylene (HDPE) [45] because of their good thermal stability, weather resistance, excellent toughness, and ageing resistance. Giant magnetoresistance (a resistance change larger than at least 1.0% upon applying an external magnetic field) has been observed in multilayered metallic structures, carbon species, conductive polymers and their nanocomposites, and conductive epoxy nanocomposites with hybrid carbon nanofibers and nanomagnetite [46–50]. However, the EOCs as the hosting polymer matrix for conductive PNCs have been rarely studied. The GMR and electron transport in the copolymer PNCs have been rarely reported either.

In the current study, EOCs with different CNTs loading levels were prepared by a surface coating method. The EOCs pellets were swelled to allow CNTs to stick on their surface. The preparation procedure was extremely mild, easy to control and repeat. Then the dried EOCs pellets coated with CNTs were pressed at different temperatures to get the PNCs final finishing. The morphology was investigated by SEM. The rheological behaviors of the nanocomposites at melt state were investigated including storage and loss moduli, steady state viscosity, and loss factor. The PNCs were studied by the XRD, DSC, and TGA. The effects of CNTs loading level and processing temperature on the electrical conductivity, optical property, and thermal conductivity were investigated. The room-temperature resistance variation as a function of magnetic field (M-R) was recorded. The electron transport mechanism was investigated by the variable range hopping approach. Both positive and negative magnetoresistance were analyzed by using wave-function shrinkage model and forward interference model, respectively.

2. Experiments

2.1. Materials

The ethylene/1-octene copolymers (EOCs) (Infuse 9500 Olefin Block Copolymer, Density: 0.878 g cm^{-3}, M_w: 82600 g mol^{-1}, M_w/M_n: 2.3, T_m: 122 °C, T_g: -45 °C) used in this research was provided by Dow Chemical Company. The carbon nanotubes (CNTs, SWeNT SMW 200X) were supplied by SouthWest NanoTechnologies, Inc with a reported average diameter of 10.4 nm and average length of 4.3 μm. Laboratory grade xylene with a reported density (ρ) of 0.87 g cm^{-3} was purchased from Fisher Scientific and served as solvent for the copolymers. No further treatment was made for all the chemicals before usage.

2.2. EOC-based nanocomposites: preparation

The EOCs-nanocomposites with 0.7, 2.0, 3.6 and 6.8 wt% CNTs loadings were prepared with a similar process as previously reported for PP nanocomposites [29]. In short, the EOCs powders were dispersed first in xylene and magnetically stirred at 50 °C for 5 h until the polymer powders were fully swelled. When their surface began to dissolve, the mixture was stirred for additional 5 h after adding CNTs to the solution. Finally, EOCs pellets coated with CNTs were obtained when extra xylene was vaporized. The final pellets were pressed into a round disk in a hot press for testing at 100, 120 and 160 °C to study the effects of physical effects from the processing temperature on the nanocomposites.

2.3. Characterizations

The rheological properties of the nanocomposites at melt state were studied with shear rates varying from 0.01 to 10 s^{-1} in a rheometer (AR 2000ex, TA Instruments) equipped with an environmental test chamber with a steel parallel-plate (25 mm in diameter) geometry to control the temperature at 170 °C. Dynamic rheological behaviors were also measured with frequency varying from 0.1 to 100 rad s^{-1} at a low strain of 1.0% (within the linear viscoelastic range). The strain-storage modulus (G′) curve was used to determine the linear viscoelastic range with the strain changing from 0.1 to 100 and a constant frequency of 1 rad/s.

A Bruker AXS D8 Discover diffractometer was used to study the crystalline structure of pure EOC and its composites. A thermogravimetric analysis (TGA, Q-500, TA Instruments) was used to evaluate the thermal stability at a 60 mL/min nitrogen and a heating rate of 10 °C/min. The evaluated temperature was adjusted from 30 to 600 °C. With a nitrogen flow rate of 20 mL/min and a heating rate of 10 °C/min, further test was done in a differential scanning calorimeter (DSC, TA Instruments Q2000). The temperature was changed from room temperature to 180 °C to eliminate the thermomechanical effect. The temperature was then lowered to room temperature and reheated back to 180 °C.

The thermal conductivity was measured by utilizing a direct measuring device (LaserComp, FOX50), capable of testing samples from −10 to 110 °C. The measureable thermal conductivity range was from 0.1 to 100 W m^{-1} K^{-1}. The samples were prepared following the requirements as designed by the ASTM C518. The specimen with flat parallel surfaces was placed between the top plate (hot surface) configured to be at a higher temperature and the bottom plate (cold surface) at lower temperature. Therefore, the heat flow went from the top to the bottom. The thickness of the specimen was measured by the equipment. Each sample was measured at an average temperature of 15, 25, 35, 45, 55, and 65 °C, respectively.

The morphology of the fracture surface was observed by a field emission scanning electron microscope (SEM, JEOL JSM-6700F). The samples were prepared by breaking the hot-pressed nanocomposites films in liquid nitrogen and coated with a thin gold coating before testing.

The UV–vis–NIR diffuse reflectance spectra (DRS) of the PNCs were recorded by A JASCO spectrophotometer (Model V-670) having a Jasco ISN-723 diffuse reflectance accessory. The samples were prepared in the same way as that for the resistivity test.

The EOCs/CNTs samples were pressed to the round shape film (2.0 mm thick) with a diameter of 25 mm under a pressure of

95 MPa in a hydraulic presser. The standard four probe method was used to measure the electrical resistivity. Magnetoresistance (MR) at 130 and 290 K was obtained by measuring the resistance as a function of field with a standard four-probe technique in a 9-T Physical Properties Measurement System (PPMS, Quantum Design).

3. Results and discussion

3.1. Melt rheological behaviors

From processing and application aspects, the rheological behavior of PNCs melts is very important since it reflects the microstructure of materials, and the polymer-nanofiller interaction. Fig. 1 presents the shear rate dependent viscosity of neat EOCs and their nanocomposite melts processed at different temperatures. Newtonian behavior was observed in all these samples together with the shear thinning (power law) behaviors under melting state. At a low shear rate, the alignment of CNTs was destroyed by random thermal motion. Meanwhile, the entanglement rebuilding of polymer chains can follow the speed of breaking the physical cross-linking. Therefore, the viscosity of PNCs is constant at low shear rates, and the region is called first Newtonian region [51]. However, the rebuilding rate becomes lower than that of breaking the physical cross-links with further increasing the shear rate, and a steady state alignment level is achieved. The viscosity would be reduced with increasing the shear rate, i.e., the shear thinning phenomenon was observed in the polymer melt. These curves clearly demonstrate a Newtonian phenomenon in the low shear rate region and a shear thinning phenomenon in the high shear rate region [52]. A constant viscosity plateau was observed indicating the Newtonian behavior of the neat EOCs and the viscosity began to decrease drastically at a shear rate larger than 1 s^{-1}, Fig. 1. However, compared with the melt of neat EOCs, the sharp reduction positions of viscosity shift to lower shear rate for the PNCs (0.1 s^{-1} for 6.8 wt% CNTs, Fig. 1c) with increasing the CNTs loading level, indicating that the nanotubes enhance the shear thinning behavior of the nanocomposites with different processing temperatures. At the same shear rate, the viscosity is increased with increasing the CNTs loading but is declined at 3.6 and 6.8 wt% CNTs. This phenomenon can be clearly observed at higher shear rates and can be explained by the following two aspects. One is from the added nanofillers in the entangled and confined systems ($h < R_g$, h is the average half-gap between the particles; R_g is the polymeric gyration radius), which result in an increased melt free volume [53,54]. Another

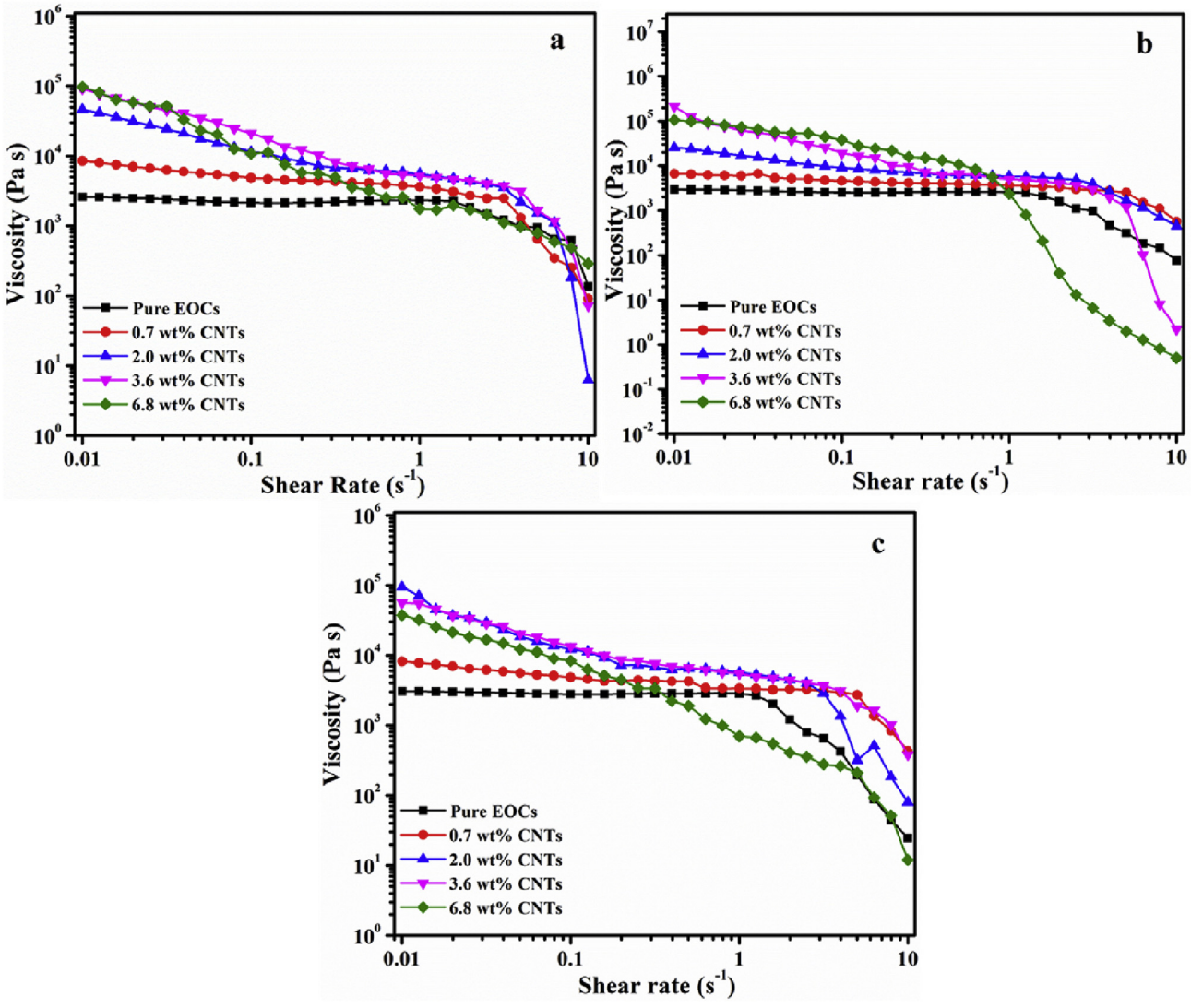

Fig. 1. Shear rate dependent viscosity of EOCs and EOCs/CNTs nanocomposites melts (measured at 170 °C) with different CNTs loadings made at (a) 100, (b) 120 and (c) 140 °C.

reason is the nanoparticle dilution effect that provides constrained release of entangled polymer chains [53]. Other composites are also observed to show stronger thinning behavior. For example, Wang et al. [55] reported that polyamide 6/poly(ethylene-1-octene) (POE) blends displayed shear thinning behavior due to the diffusion of copolymers with POE chains to the PA6 matrix.

The formed percolated systems can be perceived by studying the thermomechanical properties of the EOCs/CNTs nanocomposites melts processed at 140 °C as a function of frequency [56–58]. Fig. 2a depicts the frequency dependent G' for pure EOCs and nanocomposites melts measured at 170 °C. The observed fully relaxed EOCs chains show a typical homopolymer-like terminal behavior and disappear with increasing the CNTs loading. The observed larger enhanced G' with orders of magnitude in the low frequency range indicates that the added CNTs restrained the relaxation of polymer chains at large scale. Moreover, the G' curve of the PNCs with relatively higher CNTs contents (≥2.0 wt%) reaches a plateau in the low frequency range. This observed "plateau" represents either a strong particle-polymer interaction or an interconnected structure of fillers [57]. However, the influence of the CNTs content on the rheological behavior is relatively weak in the high frequency range, demonstrating that the influence of the CNTs on the short-range dynamics of the EOCs chains is not obvious [28]. Similar G'' curve is observed (Fig. 2b). More attention should be paid to the effects of CNTs loading on the tanδ (Fig. 2c). The tanδ (the ratio of G'' to G') is used to evaluate the composite damping. The tanδ is decreased with increasing the CNTs loading, exhibiting a corresponding flatter curve. It is the discordance between strain and stress that causes the mechanical loss in the polymer when it is subjected to an applied frequency dependent external force [59]. Meanwhile, the observed higher tanδ of neat EOCs than that of the nanocomposites is due to the full relaxation of polymer chains. The relaxation of the polymer chains and the relative motion are hardly restrained by the existing CNTs. Therefore, the friction heat from the internal chains is generated less after applying the same frequency than that of neat EOCs. In addition, the PNCs with higher CNTs loadings (≥2.0 wt%) have lower tanδ value, indicating that a strong CNTs-polymer interaction causes less friction heat loss in PNCs than that of pure EOCs [60]. A broad peak is observed on the tanδ curve and the peak position is shifted to a higher frequency. Both are due to the dissipation of energy and the relaxation of EOCs chains.

3.2. Crystallinity

Fig. 3 shows the XRD patterns of pure EOCs and its PNCs. Both

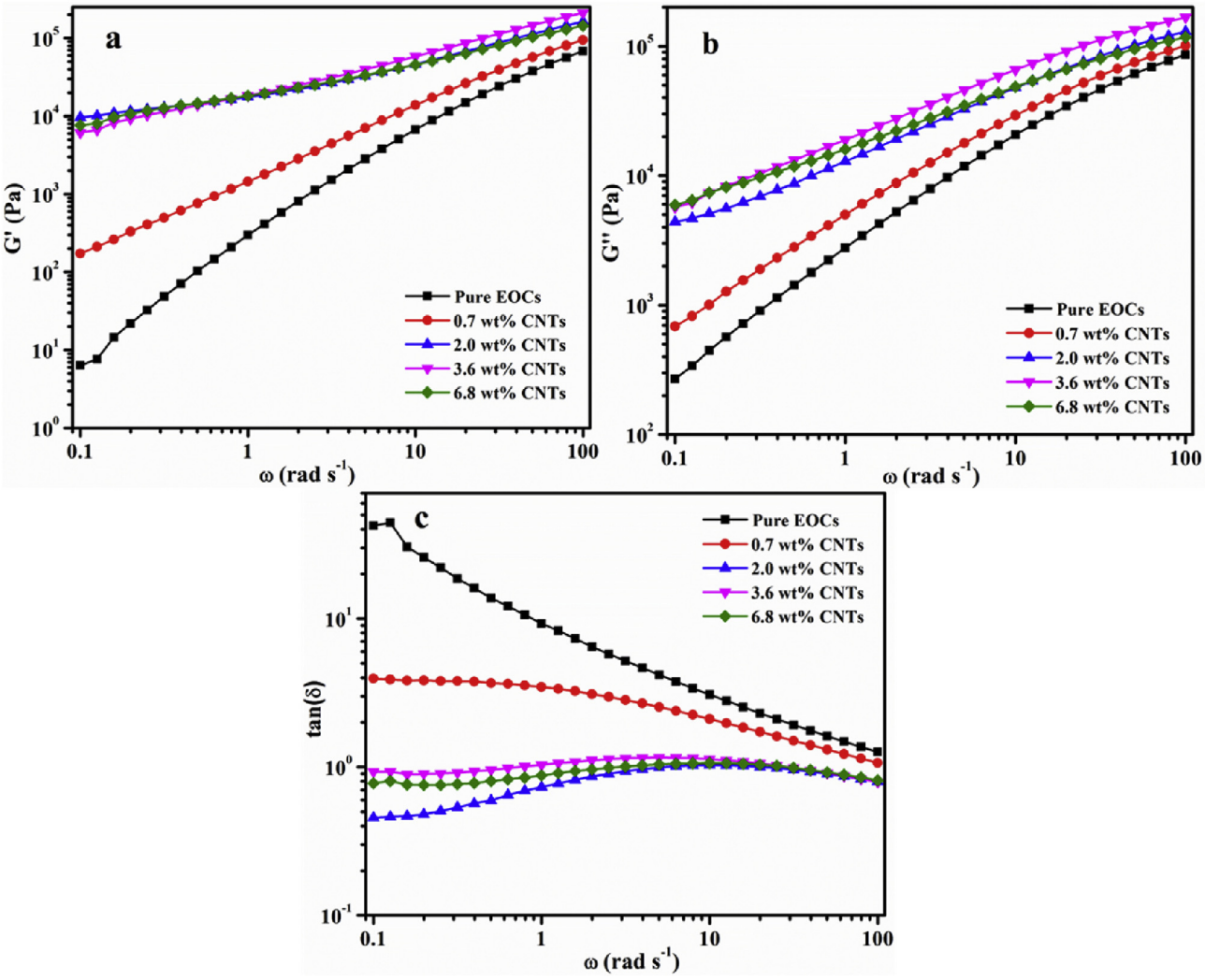

Fig. 2. Angular frequency (ω) dependent (a) Storage modulus (G'), (b) loss modulus (G''), and (c) loss factor (tanδ) of neat EOCs and EOCs/CNTs nanocomposites melts (measured at 170 °C) with different CNTs loadings processed at 140 °C.

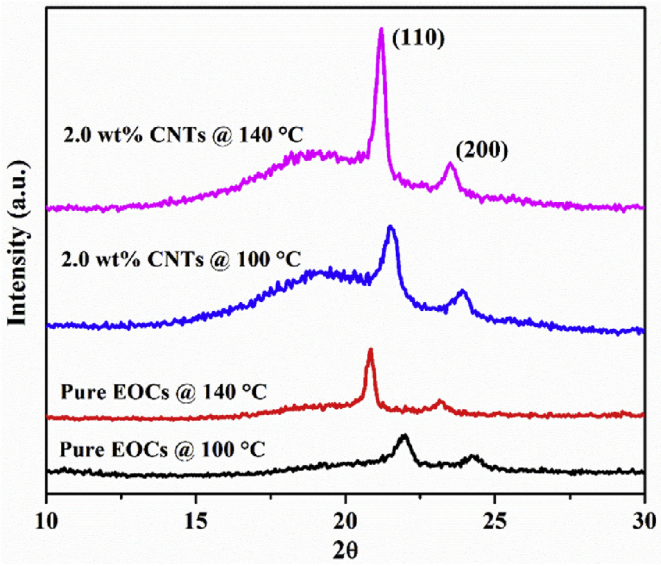

Fig. 3. XRD curves of EOCs processed at 100 and 140 °C, and the2.0 wt% CNT nanocomposites made at 100 and 140 °C.

mainly exhibit a strong reflection peak followed by a weaker peak, ascribing to the typical orthorhombic unit structure of the (*110*) and (*200*) reflection planes [61,62]. It is worth noting that the peak minimum positions of the (*110*) and (*200*) are detected at 20.8° and 23.1° for pure EOCs processed at 140 °C, which shift to lower angles compared with that of EOCs processed at 100 °C. It can also be observed from that of 2.0 wt% nanotube PNCs pressed at 100 and 140 °C. The CNTs affect the crystallite of EOCs. For the crystalline materials, Bragg formula is used to calculate the lattice *d*-spacing, Equation (1) [63],

$$n\lambda = 2d \cdot \sin\theta \quad (1)$$

where *n* is chosen as 1 and λ is the X-ray wavelength ($\lambda = 1.5406$ Å) and θ is the diffraction angle. When the θ becomes smaller, the d-spacing will become larger, implying that the increased processing temperature results in an increased effect of the side chains on the crystal phase. But the peak positions of nanocomposites with 2.0 wt % pressed at 140 °C are shifted to higher angles than that of pure EOCs processed at the same temperature. It appears that the CNTs can prohibit the release of copolymer side-chains in the matrix. Moreover, with a higher processing temperature and the introduction of CNTs, the PNCs with 2.0 wt% CNT loading processed at 140 °C have the highest intensity of these two peaks, arising from the crystalline phase and the large decrease of the half-width of amorphous halo [62].

The Scherrer Equation was used to calculate the average crystallite size, Equation (2) [64],

$$L = \frac{k\lambda}{\beta \cos\theta} \quad (2)$$

where *L* is the average crystallite size, *k* is the shape factor, β is the full width at half maximum, and θ is the angle at maximum intensity. The *k* value depends on the Miller index of reflection plane, the shape of crystal (normally 0.89 if the shape is unknown) and other factors. Here, the $2\theta = 21.2°$ peak of the 2.0 wt% CNTs PNCs is used to calculate and it is about 24.05 nm.

3.3. Thermal stability and thermal behaviors

Fig. 4 shows the thermal stability of neat EOCs and composites. For all the samples, there is A sharp weight loss was observed in the temperature range from 380 to 510 °C for all the samples, consistent with the observation in Ketloy's study [65]. Compared with that of pure EOCs, the temperatures of the onset degradation (T_{on}) and 10% mass loss ($T_{10\%}$) are observed to slightly increase with increasing the CNTs loading except the nanocomposites with 6.8 wt % CNTs, Table 1, showing the stabilization of EOCs by the introduced CNTs. However, when the CNTs loading reaches 6.8 wt%, the T_{on} and $T_{10\%}$ decrease arising from high thermal conductivity of CNTs that can transfer heat to the inner part of polymer more quickly. With a careful study of the DTG curves, two peaks in the range from 425 to 500 °C for the PNCs are observed after introducing CNTs, Fig. 4b, which are due to the strong interfacial interaction between the particle and polymer [66]. However, the interfacial interaction is destroyed more quickly in the nanocomposites with increasing the CNTs content; therefore, the 6.7 wt% CNTs PNCs show one peak. Although lots of nanomaterials such as nanoclays [67] and silica nanoparticles [68] were used to enhance the thermal stability, only small increase (typically less than 50 °C) was achieved. This thermal stability of the PNCs in N_2 synthesized by surface coating approach may supply some guidance to the rational design of thermally

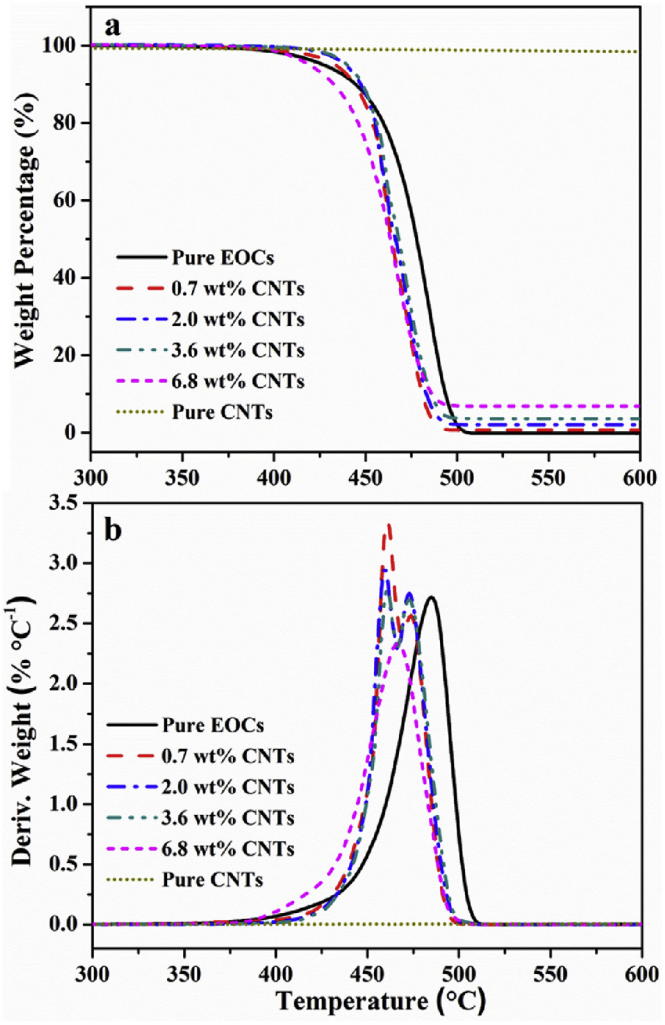

Fig. 4. a) TGA and b) DTG curve of copolymer and nanocomposites with a nanotube content of 0.7, 2.0, 3.6 and 6.8 wt%, and pure CNTs.

Table 1
TGA data of pure copolymer and PNCs.

CNT loading (wt%)	Neat copolymer	0.7 wt%	2.0 wt%	3.6 wt%	6.8 wt%
T_{on} [°C]	405	415	427	429	405
$T_{10\%}$ [°C]	444	444	447	448	432

stable composites.

The comonomer was introduced as short side chain branches and influence the microstructure, crystallization, and final shapes of the final copolymers. Their crystallization and melting behaviors are complicated as revealed by several melting endotherms in the DSC results. Fig. 5 shows the DSC curves of pure EOCs and composites. The exact crystalline peak temperature, T_c; enthalpy of the crystallization, ΔH_c; melting peak temperature, T_m; enthalpy of the fusion, ΔH_m; and crystalline fraction, F_c, are summarized in Table 2. The ΔH_c and ΔH_m fusion are obtained by directly integrating from the DSC graphs. The first cooling and second heating processes are carried out to study the crystalline behavior and thermal history effect on the performances of the composites. The pristine EOCs exhibited a T_c of 99.06 °C and a T_m of 122.04 °C. The introduction of α-olefins to the polyethylene chain led to a decreased regularity in the chain structure and resulted in a lower crystallinity, density, and crystallizing and melting points [69–71]. Therefore, such copolymers have properties that differ from the homopolyethylene. Moreover, for the first cooling process, an increased CNTs content is observed to result in a shift of T_c to lower temperatures, since the nanofillers restrained the movement of polymer chains. However, the T_c of HDPE/Fe@FeO core-shell system [72] is similar to that of neat HDPE, revealing that the introduced nanoparticles did not change the original crystal structure of the matrix. For the second heating process, the T_m of PNCs is observed to be almost the same as that of pure EOCs, indicating that introduced CNTs by surface coating method did not change the original crystal structure of the hosting polymer. However, the ΔH_m of pure EOCs was decreased from 48.19 to 40.06 J/g when 0.7 wt% CNTs were introduced in EOCs; and decreased to 30.02 J/g further in the composites with 6.8 wt%. The F_c of pure EOCs and nanocomposites can be calculated from Equation (3) [73],

$$F_c = \frac{\Delta H_m}{\Delta H_m^0 \times (1 - x)} \tag{3}$$

where ΔH_m is the enthalpy of the samples (J/g), and ΔH_m^0 is the enthalpy for a theoretical orthorhombic polyethylene 288.4 (J/g) [74] and x is the CNTs loading. From the results summarized in Table 2, the F_c is observed to be decreased slightly (2–3%) after the CNTs were introduced into the hosting EOCs. The lower F_c of these PNCs is attributed to the CNTs that destroy the continuous EOCs chains. As a result, more grain boundaries and defects were introduced in the EOCs and suppressed the crystallinity.

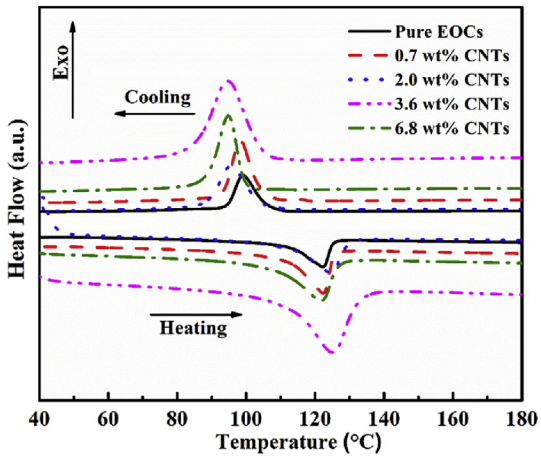

Fig. 5. DSC curves of copolymer and nanocomposites with a CNTs content of 0.7, 2.0, 3.6 and 6.8 wt%.

Table 2
Major parameters from DSC for pure copolymer and its nanocomposites.

CNTs loading (wt%)	T_c (°C)	ΔH_c (J g^{-1})	T_m (°C)	ΔH_m (J g^{-1})	F_c (%)
Pure copolymer	99.06	43.33	122.04	48.19	16.71
0.7 wt% CNTs	98.35	36.04	122.04	40.06	13.99
2.0 wt% CNTs	95.59	35.93	124.59	39.11	13.84
3.6 wt% CNTs	94.89	35.76	124.98	35.85	12.89
6.8 wt% CNTs	94.86	34.72	123.05	30.02	11.17

3.4. Thermal conductivity (λ)

The λ indicates the ability of a material for heat transfer [75]. Thermally conductive polymer nanocomposites provide alternatives to replace metal parts in various applications that require high heat dissipation, low thermal expansion, such as generators, heat exchangers and power electronics, etc. [76–78] At present, the most efficient way to improve the λ of polymers is focused on selectively adding thermally conductive fillers. The CNTs seems promising nanofillers, coupling with high λ and light weight [79,80]. The normal principle of the FOX heat flow meter instruments is based on 1-D equation for Fourier-Biot law, Equation (4) [75],

$$Q = -\lambda\,(dT/dx) \tag{4}$$

where Q is heat flux (W/m^2) flowing through the sample; λ is the thermal conductivity (W/mK) of the sample; dT/dx is the temperature gradient (K/m) on the isotherm flat surface in the sample. The thermal resistance (R, m^2 K W^{-1}) of the flat samples equals to its thickness (Δx, m) divided by its λ as shown in Equation (5):

$$R = \Delta x/\lambda \tag{5}$$

Fig. 6 shows the temperature dependent λ and R curves of neat EOCs and composites. The PNCs with 3.6 wt% CNTs pressed at 120 and 140 °C exhibited higher λ than that of pure EOCs. Meanwhile, the composites with 3.6 wt% CNTs pressed at 140 °C demonstrated higher λ than that of nanocomposites pressed at 120 °C, arising from different CNTs network structures formed at different temperatures. Hence, the PNCs with 3.6 wt% CNTs processed at 140 °C showed the lowest R than that of others, Fig. 6b. However, the λ values of composites with 0.7 wt% CNTs pressed at 100 and 140 °C are relatively lower than that of pure polymer matrix. Moisala et al. also reported that the SWNTs composites exhibited an initially decreased λ below that of neat polymer in the composites with a nanotube loading of within 0–0.5 wt% [81]. For the relative low CNTs loading, the main critical issue is that the interfacial R caused by the phonons mismatch at the CNTs-polymer interface leads to a high interface R, resulting in serious scattering of the phonons at the interface and a large reduction of thermal transport [82]. Therefore, the well formed CNTs network can enhance the λ.

3.5. Electronic property of EOCs/CNTs nanocomposites

The electronic property is one important property of a material for the applications including thin film transistor [83], solar cell

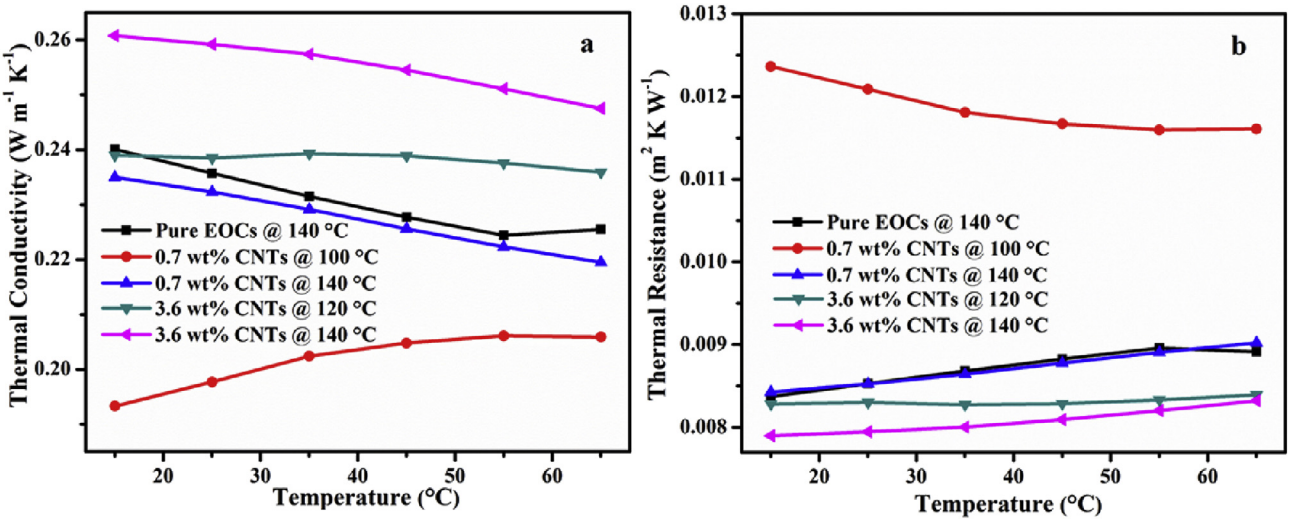

Fig. 6. a) Thermal conductivity and b) thermal resistance of EOCs processed at 140 °C, and 0.7 wt% CNTs nanocomposites made at 100 and 140 °C, 3.6 wt% CNTs nanocomposites made at 120 and 140 °C.

[84], and chemical/biochemical sensor [85]. The optical property of pure CNTs and the nanocomposites was investigated by the UV–vis spectra. The band gap (E_g) value of a sphere was calculated from a photon-energy ($h\upsilon$) dependent $\alpha h\upsilon$ obtained from the diffuse reflectance UV–Vis spectra by using Equation (6) (Tauc's plot [86]),

$$\alpha h\upsilon = \left(h\upsilon - E_g\right)^n \tag{6}$$

where α,h andυ are the coefficient of the absorbance, Planck's constant and photon frequency. The Tauc plot was obtained by converting from the diffuse reflectance UV–vis spectrum. The parameter n is a pure number related to the transition types of electrons (n = 0.5, and = 2 for the allowed direct, and indirect transitions, respectively) [87,88]. For CNTs, the reported n was ~2 [89] and the E_g was calculated by extrapolating from the energy axis in the linear part of the curve. The calculated E_g of pure CNTs was ~1.50 eV, Fig. 7a, comparable to the 1.543 eV reported for the transition above the second pair of van Hove singularity and lower than the Fermi level of carbon nanotubes with an index of (9,8) [90].

The 6.8 wt% PNCs processed at 100 °C show a much lower band gap of 0.86 eV, Fig. 7c, suitable for using as semiconductors [91]. This phenomenon can be interpreted from the point of electron quantum states. According to the Pauli exclusion principle, the electrons can be classified into state zero or state one [92]. The σ takes place arising from the existing electrons in the delocalized states. An orbital must be partly filled with electrons; otherwise, with a full filling, the orbital is inert to block the transport of other electrons. Appropriately partly filled states and the delocalization state, arising from the formed network of CNTs, led to a lower E_g. Moreover, with the same loading of CNTs (Fig. 7d&e, c&f), the E_g of the nanocomposites is dependent on the pressing temperature. The E_g variance is possibly due to the hot-press induced strain of CNTs. The strain effect on the E_g of CNTs is complex since the CNTs strain could play a positive or negative role in the electron transportation. The strain can lead to the insulating-conduction transition of SWNT arising from the varied quantum number [93,94]. However, uni-axial strain in graphene causes the red shift of 2D and G band, arising from the elongation of C–C bonds [95]. For the EOCs/CNTs system, the E_g is reduced at a higher CNT content (Fig. 7b,d&f). The changing trend of E_g corresponds to the σ value in the PNCs; i.e., the nanocomposites with higher σ showed a reduced E_g.

3.6. Electrical conductivity (σ) of EOCs/CNTs nanocomposites

Fig. 8 shows the σ variation of the nanocomposites at different CNTs loadings with different processing temperatures. The σ is increased with increasing the CNTs content, and the 6.8 wt% CNTs nanocomposites pressed at 100 °C show the highest σ of 0.015 S/cm, three orders of magnitude larger than that of the PP nanocomposites even with 5 wt% CNT loading [96]. The higher σ was ascribed to the formed conductive CNT network. At 100 °C, the EOCs pellets coated with CNTs just start to melt. The pellets would only change the shape without destroying the CNT coating during the hot press, and the CNTs would be pressed together, Scheme 1(a). At 120 °C, the pellets were under melting state, and the CNTs layer on the surface was easier to be broken and moved to the matrix, Scheme 1(b). Therefore, some parts of the CNTs network were destroyed. However, at 140 °C, the PNCs were totally molten, and more CNTs were released from the layer and diffused into the polymer matrix. The network still existed, but the density of network was lower than that at 100 °C, Scheme 1(c). These can well explain the lower σ in the 6.8 wt% CNTs PNCs processed at 140 °C than that processed at 100 °C, and higher σ than that processed at 120 °C. This can be verified by the morphological study, Fig. 9. For the 2.0 wt% CNT nanocomposites prepared at 100 °C, the pellets were observed with surface deformed and coated with CNTs, Fig. 9a. The network structure is observed with 2.0 wt% CNTs in PNCs pressed at 100 °C, indicating a low percolation concentration for the PNCs [97]. The CNTs are observed to agglomerate to form network structures, Fig. 9b–c, thereby leading to a sharp increase in the σ. However, for the nanocomposites made at 120 °C, the CNTs coating wss separated by EOCs since the matrix began to melt, Fig. 9c. The conducting paths were arisen from the CNTs. At increased temperatures (for example, 120 and 140 °C), since the diffusion of the CNTs to the EOCs matrix caused the dispersion of the CNTs, and limited CNTs can form conductive path, Fig. 9c–d [98]. However, the network density rises since more nanotubes involve in the formation of conductive network, when the PNCs were prepared

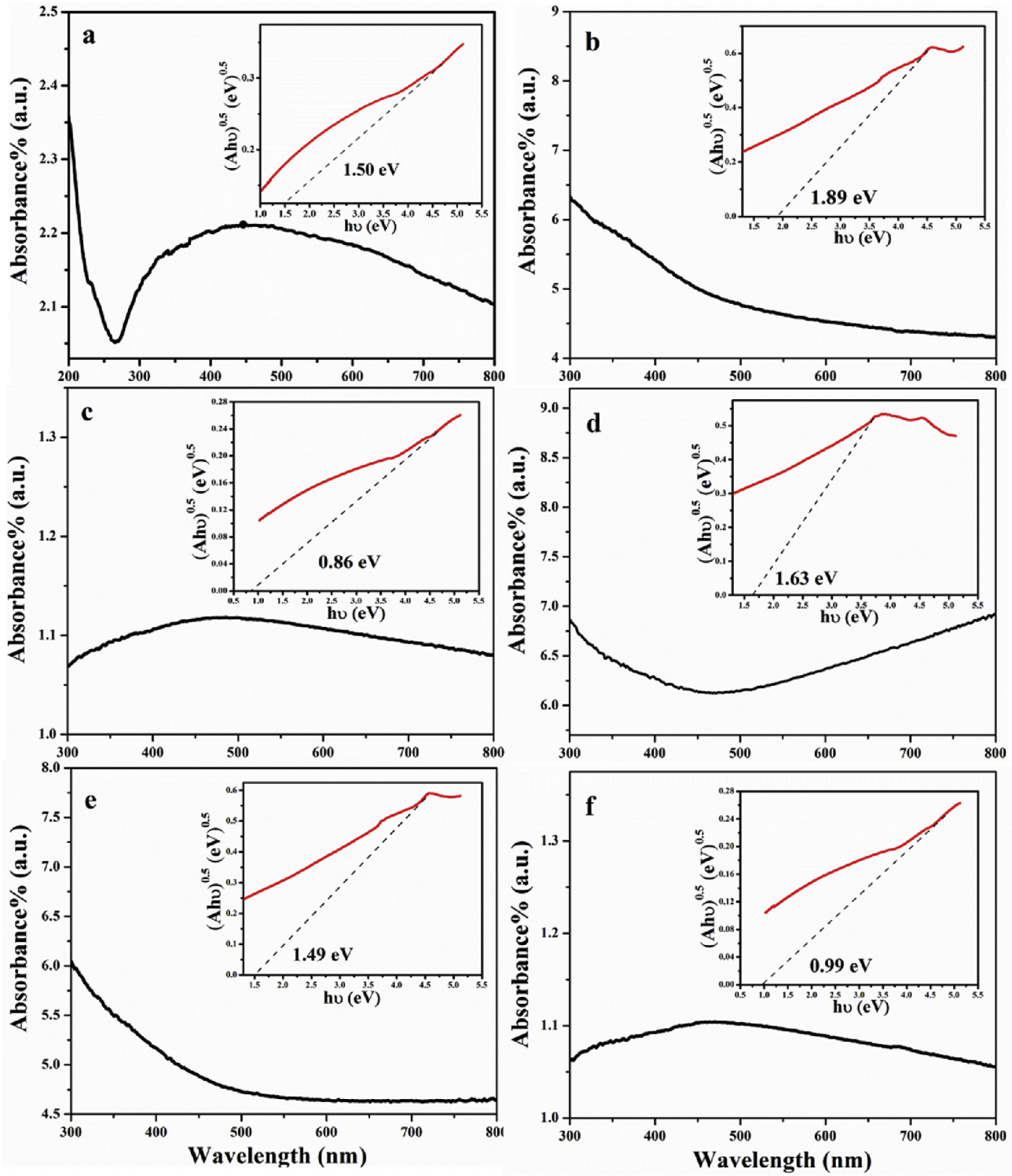

Fig. 7. UV–vis absorbance spectrum (converted from diffuse reflectance spectrum data) of: a) nanotubes; Nanocomposites made at 120 °C with b) 2.0, d) 3.6 and f) 6.8 wt% CNTs loadings; c) nanocomposites made at 100 °C with 6.8 wt% CNTs loadings; e) nanocomposites made at 140 °C with 3.6 wt% CNTs content. The insets depict the Figure to obtain the bandgap for a direct bandgap transition for a-f, respectively.

at low temperature (100 °C), leading to a higher σ [98].

3.7. Temperature dependent resistivity – electrical conductivity mechanism

Fig. 10a shows the temperature dependent resistivity for the nanocomposites with 2.6 and 3.0 wt% CNTs made at 120 and 140 °C. For all the samples, the resistivity is decreased with the increase of the temperature, indicating a semiconducting behavior within the measured 45–220 K region [99]. The PNCs obey the following resistivity changing trend: 2.0 wt% CNTs@120 °C > 2.0 wt% CNTs@140 °C > 3.6 wt% CNTs@120 °C > 3.6 wt% CNTs@140 °C. The resistivity is observed to follow the variable range hopping (VRH) theory, which depends on the network structure in the polymer

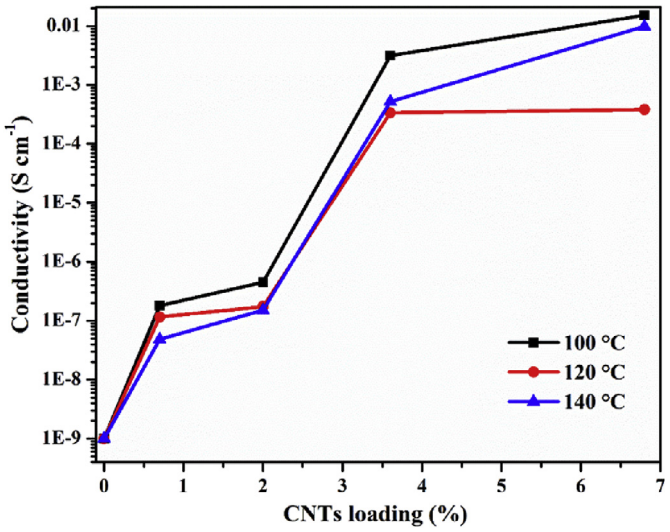

Fig. 8. CNTs loading dependent electrical conductivity of nanocomposites for the samples made at 100, 120 and 140 °C.

matrix. The electron transport mechanism was exploited by the temperature-σ VRH relationship, Equation (7) [100],

$$\sigma = \sigma_0 \exp\left[-\left(\frac{T_0}{T}\right)^{1/(n+1)}\right] \tag{7}$$

where the constant T_0 (K) is the characteristic Mott temperature associated with the electronic wave function localization degree, σ_0 is the conductivity at infinite low temperature, T is the Kelvin temperature, and n can be 1, 2 and 3, standing for one-, two-, and three-dimensional systems, respectively. Fig. 10b shows the best linear fits of $\ln(\sigma) \sim T^{-1/(n+1)}$ for PNCs (Fig. 10a) with n = 3 in 45–220 K range. This indicates a 3-d electron transport mechanism. This means that the PNC systems with 2.6 and 3.0 wt% nanotubes respectively made at 120 and 140 °C are disordered in the 3-d VRH regime. The T_0 and σ_0 values can be calculated from the intercept, and slope of the plot $\ln(\sigma) \sim T^{-1/(n+1)}$, and Table 3 shows the summarized results. The T_0 value of the composites obeys the following order: 2.0 wt% CNTs@120 °C > 2.0 wt% CNTs@140 °C > 3.6 wt% CNTs@120 °C > 3.6 wt% CNTs@140 °C, which is consistent with the measured resistivity values. The σ_0 rises with the decrease of the processing temperature within a certain CNT loading. In general, a larger T_0 indicates a stronger localization of the charge carriers in the system and thus represents a lower σ [101]. Therefore, these results also prove that although the nanofillers have free movement in the matrix at higher temperature, the network is still formed with lower density of CNTs.

3.8. Magnetoresistance (MR)

Fig. 11 shows the magnetoresistance (MR) of 2.6 wt% nanotubes reinforced nanocomposites made at 120 °C, and 3.0 wt% nanotubes PNCs pressed at 140 °C. The MR is calculated using Equation (8) [102],

$$\mathrm{MR\%} = \frac{\mathrm{R}(H,T) - \mathrm{R}(0,T)}{\mathrm{R}(0)} \times 100 \tag{8}$$

where *R (0, T)* and *R (H, T)* are the resistance with zero field and under a magnetic field *H*. The MR results show different field dependent behaviors and can be classified to two groups. The first is the relatively large positive MR measured at 290 K (red curves), the other is negative MR from PNCs measured at 130 K (black curves). The positive MR is due to the shrinkage in the overlap of wave function of the electrons after applying a field and thus a decreased average hopping length [103]. The wave function shrinkage model is normally used to depict the positive magnetoresistance and the R(H,T)/R(0,T) ratio can be expressed as Equation (9) [104],

$$R(H,T)/R(0,T) = \exp\{\xi_C(0)[\xi_C(H)/\xi(0) - 1]\} \tag{9}$$

where $\xi_C(0) = (T_0/T)^{1/4}$ for the 3 dimensional Mott VRH transport;$\xi_C(H)/\xi_C(0)$ is H/P_C *dependent* normalized hopping probability parameter for the Mott VRH charge transport mechanism; *H* is the field (Tesla, 1 T = 10^4 Oe, T = kg C^{-1} s^{-1}); The fitting parameter P_C, the normalizing field to be extracted from the MR ratios, is calculated by Equation (10) for the Mott VRH transportation [104,105],

$$P_C = 6\hbar \Big/ \left[e a_0^2 (T_0/T)^{1/4}\right] \tag{10}$$

where e is electron charge ($1.6021765 \times 10^{-19}$), $\hbar$ is the reduced Planck's constant, and $\hbar = \mathrm{h}/2\pi$, h is the Planck's constant. With low field limit especially considering the non-magnetic materials, Equation (10) is simplified to Equation (11),

$$R(H,T)/R(0,T) \approx 1 + t_2 \frac{H^2}{P_C^2}\left(\frac{T_0}{T}\right)^{1/4} \tag{11}$$

And MR is defined as Equation (12),

$$\mathrm{MR} = \frac{R(H,T) - R(0,T)}{R(0,T)} \approx t_2 \frac{H^2}{P_C^2}\left(\frac{T_0}{T}\right)^{1/4} = t_2 \frac{e^2 a_0^4}{36\hbar^2}\left(\frac{T_0}{T}\right)^{3/4} H^2 \tag{12}$$

where the numerical constant $t_2 = 5/2016$.

According to Equation (12), the localization length a_0 can be calculated by Equation (12) from T_0, MR values, and H:

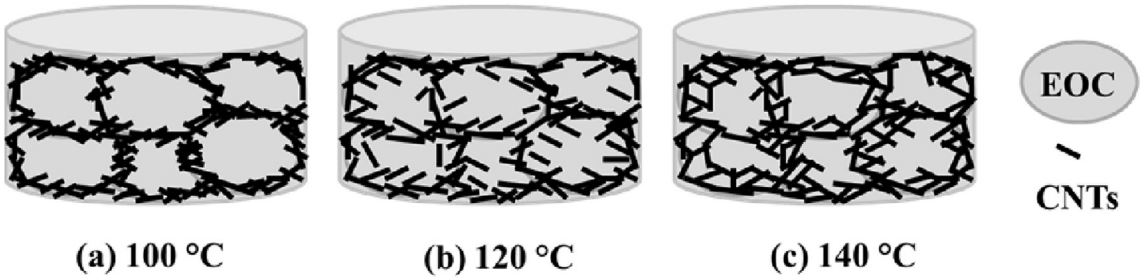

Scheme 1. The morphology of nanocomposites at different pressing temperatures (not scaled).

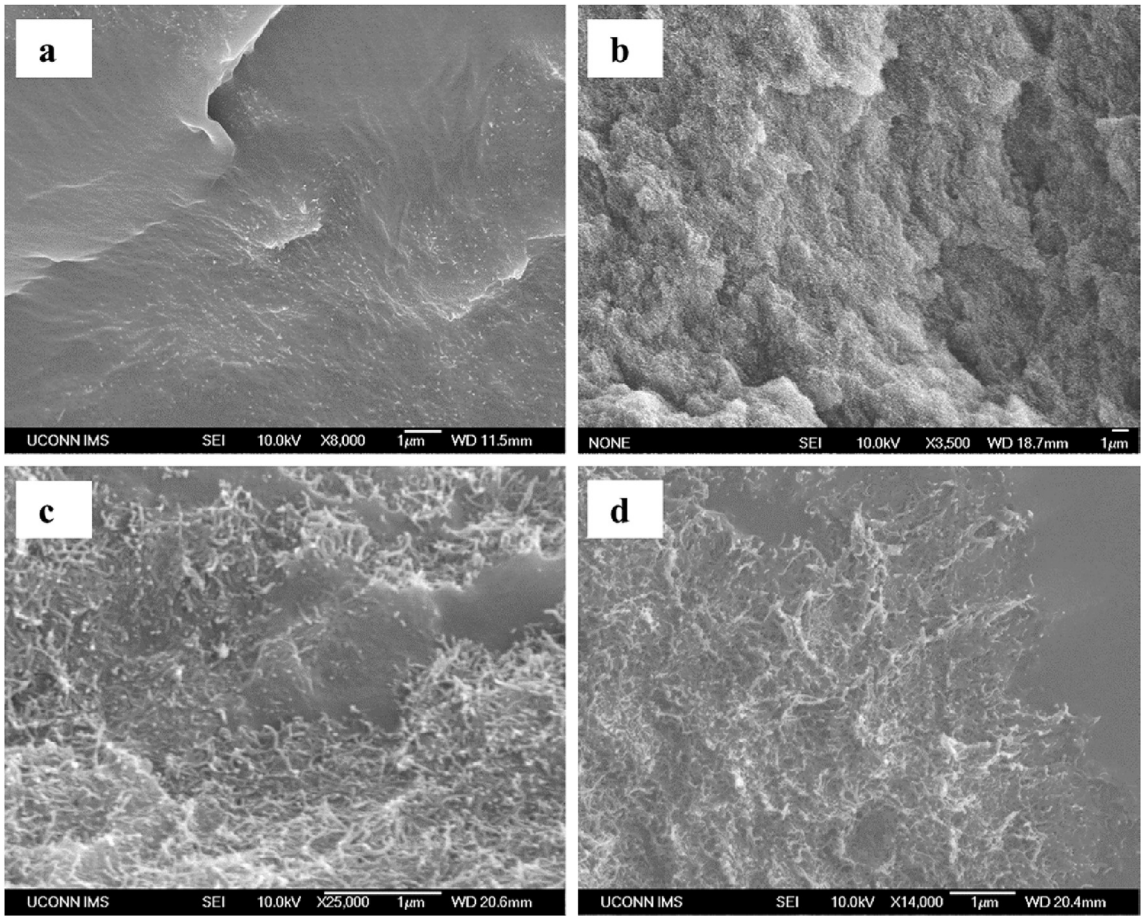

Fig. 9. SEM graphs of nanocomposites with 2.0 wt% CNTs made at a) 100 °C and nanocomposites with 6.8 wt% CNTs made at b) 100, c) 120 and d) 140 °C.

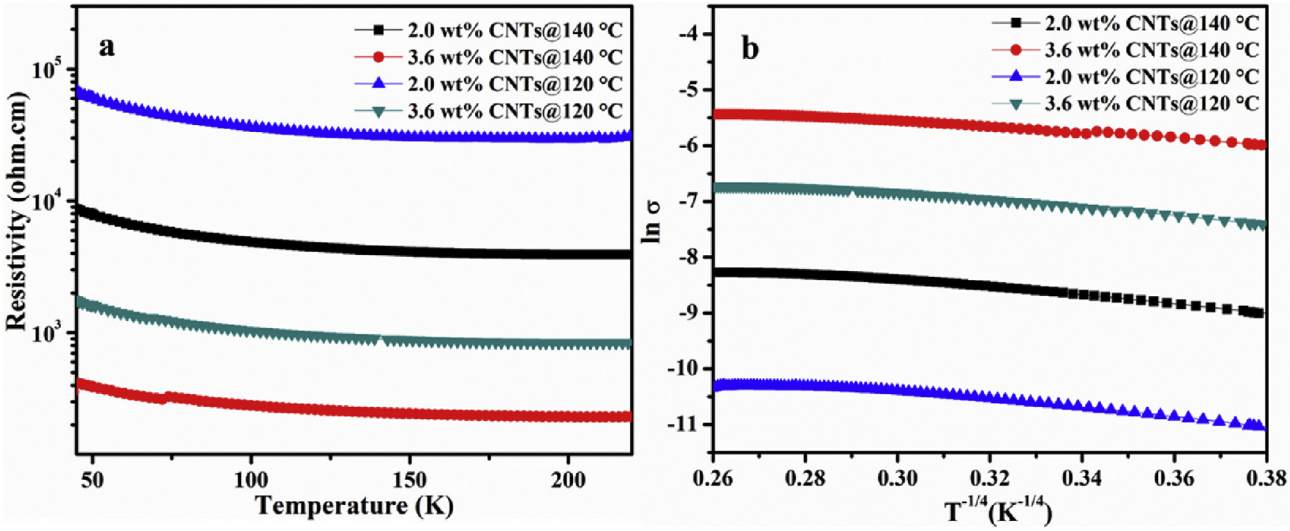

Fig. 10. a) Temperature dependent resistivity, and b) ln(σ) vs $T^{-1/4}$ curves of CNTs nanocomposites.

Table 3
T_0 and σ_0 for the EOCs/CNTs PNCs.

Samples	T_0 (K)	$\sigma_0 \times 10^4$ (S/cm)
2.0 wt% CNTs@120 °C	2868.05	2.75
2.0 wt% CNTs@140 °C	2138.57	17.36
3.6 wt% CNTs@120 °C	2076.80	80.61
3.6 wt% CNTs@140 °C	1087.84	216.43

$$a_0^4 = \frac{36\hbar^2 MR}{t_2 e^2}\left(\frac{T_0}{T}\right)^{-3/4} H^{-2} \quad (13)$$

The calculated a_0 of EOCs/CNTs PNCs is listed in Table 4. The a_0 is observed to be decreased with the increase of the H; and the higher

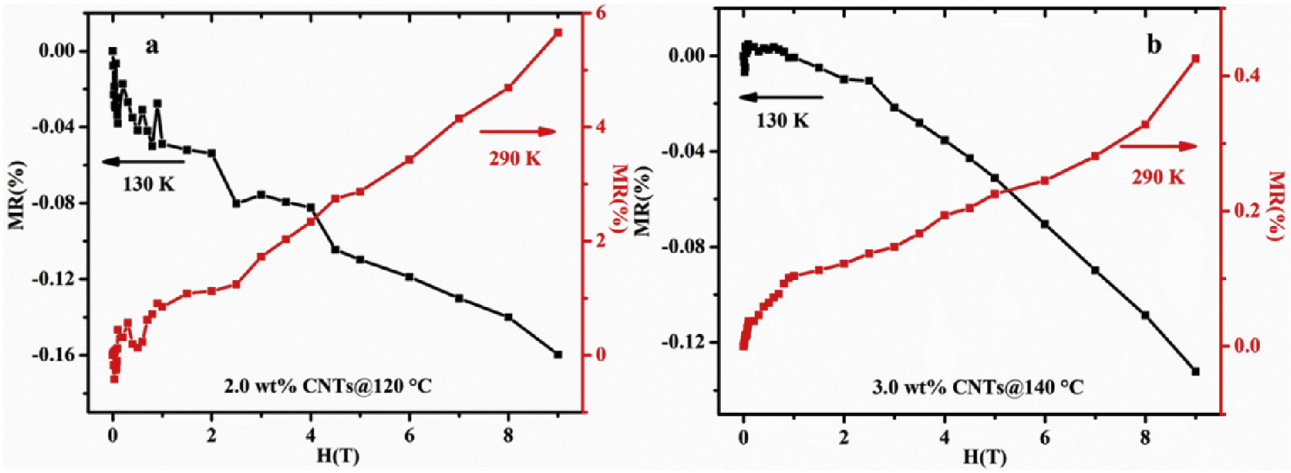

Fig. 11. Magnetoresistance of nanocomposites with a CNTs loading of a) 2.6 wt% processed at 120 °C, and b) 3.0 wt% processed at 140 °C. The MR was measured at 130 and 290 K.

Table 4
The a_0 for EOCs/CNTs PNCs at different magnetic fields *H*.

Samples	Parameters	Magnetic field (*H*, *T*)		
		1	4	9
2.0 wt% CNTs@120 °C	a_0 (nm)	55.62	35.83	29.79
	R_{hop} (nm)	36.99	23.83	19.81
3.6 wt% CNTs@140 °C	a_0 (nm)	39.49	23.06	18.71
	R_{hop} (nm)	20.61	12.03	9.76

MR accompanies with a smaller a_0. The R_{hop} (average hopping length) can be calculated from Equation (14) by T_0, T and a_0 [106],

$$R_{hop} = (3/8)(T_0/T)^{1/4}a_0 \quad (14)$$

Table 4 summarizes the calculated R_{hop}, which is H dependent. In a hopping system, the magnetoresistance comes from the charge hopping conduction due to the wave function contraction of the charge carriers and the following decreased R_{hop} [107]. Thus, the R_{hop} is decreased with the increase of the *H* and the MR rises with the increase of the H, indicating that the MR value is related to the R_{hop}.

The negative magnetoresistance effect of these nanocomposites can be interpreted by the orbital magnetoconductivity theory [47]. The interferences among these hopping paths were considered in this theory. The conducting paths will include a series of scattering for the tunneling electrons by the impurities that are located within the cigar shape domain with a length of r_h and a width of $(r_h a_0)^{1/2}$ [108]. The negative MR decreases with the increase of the *H*. At 130 K, the MR of nanocomposites with 2.0 wt% CNTs prepared at 120 °C and with 3.0 wt% CNTs made at 140 °C are −0.16% and −0.12%, respectively. The negative MR is also obtained in the bulk samples of SWCNTs [109]. The lower measured temperature causes a reduced resistance of CNTs network, causing a negative magnetoresistance. This MR switching phenomenon with different temperature demonstrated in these nanocomposites provides a great opportunity to obtain MR with desired values.

4. Conclusions

Ethylene/1-octene copolymers (EOCs) nanocomposites with different loading levels of CNTs were prepared by sticking the CNTs on the gelated EOCs pellet surface. A strong CNTs-polymer interaction led to a less friction heat loss in the PNCs than pure EOCs. The SEM observations showed that the CNTs were pressed tighter and a network structure was formed and gave a higher electrical conductivity. Both XRD and DSC results revealed a constant crystalline structure of EOCs during the synthesis of EOCs PNCs. The CNTs played as heat transfer medium in the matrix, depending on the CNTs loading level. All pure EOCs and the PNCs revealed both Newtonian and shear thinning (power law) behaviors under melting states. The observed rheological plateau in the low oscillation frequency region was duo to the formed network of CNTs in the hosting EOCs matrix. Finally, the varying trend of E_g in these nanocomposites corresponds to the σ value of PNCs, the nanocomposites with higher σ showed a lower E_g. Variable range hopping revealed a 3-d electron transport in the PNCs with 2.6 and 3.0 wt% nanotubes respectively made at 120 and 140 °C. Both positive and negative MR can be obtained by fabricating PNCs at different temperatures, offering a promising approach to achieve desired MR devices.

Acknowledgements

The authors appreciate the financial supports from American Chemical Society Petroleum Research Fund (ACS PRF# 53930-ND6) and the start-up funds from University of Tennessee (No. E01-1320-022). D. P. Young acknowledges the support from the NSF under Grant No. DMR 13-06392, the National Natural Science Foundation of China (No. 51403175); Shaanxi Natural Science Foundation of Shaanxi Province (No. 2015JM5153) and the Fundamental Research Funds for the Central Universities (No. 3102015ZY066).

References

[1] X. Zhang, X. Yan, J. Guo, Z. Liu, D. Jiang, Q. He, H. Wei, H. Gu, H.A. Colorado, X. Zhang, S. Wei, Z. Guo, Polypyrrole doped epoxy resin nanocomposites with enhanced mechanical properties and reduced flammability, J. Mater. Chem. C 3 (2015) 162–176.
[2] Q. He, T. Yuan, X. Zhang, X. Yan, J. Guo, D. Ding, M.A. Khan, D.P. Young, A. Khasanov, Z. Luo, J. Liu, T. Shen, X. Liu, S. Wei, Z. Guo, Electromagnetic field absorbing polypropylene nanocomposites with tuned permittivity and permeability by nanoiron and carbon nanotubes, J. Phys. Chem. C 118 (2014) 24784–24796.
[3] H. Gu, J. Guo, X. Yan, H. Wei, X. Zhang, J. Liu, Y. Huang, S. Wei, Z. Guo, Electrical transport and magnetoresistance in advanced polyaniline nanostructures and nanocomposites, Polymer 55 (2014) 4405–4419.
[4] L. Sun, G.L. Warren, H.-J. Sue, Partially cured epoxy/SWCNT thin films for the reinforcement of vacuum-assisted resin-transfer-molded composites, Carbon 48 (2010) 2364–2367.
[5] P. Ajayan, O. Stephan, C. Colliex, D. Trauth, Aligned carbon nanotube arrays formed by cutting a polymer resin-nanotube composite, Science 265 (1994)

1212–1214.
[6] A.S. Aricò, P. Bruce, B. Scrosati, J.-M. Tarascon, W. Van Schalkwijk, Nanostructured materials for advanced energy conversion and storage devices, Nat. Mater 4 (2005) 366–377.
[7] A. Rudge, J. Davey, I. Raistrick, S. Gottesfeld, J.P. Ferraris, Conducting polymers as active materials in electrochemical capacitors, J. Power Sources 47 (1994) 89–107.
[8] J. Zhu, H. Gu, Z. Luo, N. Haldolaarachige, D.P. Young, S. Wei, Z. Guo, Carbon nanostructure-derived polyaniline metacomposites: electrical, dielectric, and giant magnetoresistive properties, Langmuir 28 (2012) 10246–10255.
[9] H. Gu, J. Guo, H. Wei, Y. Huang, C. Zhao, Y. Li, Q. Wu, N. Haldolaarachchige, D.P. Young, S. Wei, Z. Guo, Giant magnetoresistance in non-magnetic phosphoric acid doped polyaniline silicon nanocomposites with higher magnetic field sensing sensitivity, Phys. Chem. Chem. Phys. 15 (2013) 10866–10875.
[10] H. Gu, J. Guo, X. Zhang, Q. He, Y. Huang, H.A. Colorado, N. Haldolaarachchige, H. Xin, D.P. Young, S. Wei, Z. Guo, Giant magnetoresistive phosphoric acid doped polyaniline-silica nanocomposites, J. Phys. Chem. C 117 (2013) 6426–6436.
[11] L.J. Lee, C. Zeng, X. Cao, X. Han, J. Shen, G. Xu, Polymer nanocomposite foams, Compos. Sci. Technol. 65 (2005) 2344–2363.
[12] R. Rahimi, M. Ochoa, W. Yu, B. Ziaie, Highly stretchable and sensitive unidirectional strain sensor via laser carbonization, ACS Appl. Mater. Interfaces 7 (2015) 4463–4470.
[13] M. Amjadi, A. Pichitpajongkit, S. Lee, S. Ryu, I. Park, Highly stretchable and sensitive strain sensor based on silver nanowire–elastomer nanocomposite, ACS Nano 8 (2014) 5154–5163.
[14] T. Kashiwagi, E. Grulke, J. Hilding, K. Groth, R. Harris, K. Butler, J. Shields, S. Kharchenko, J. Douglas, Thermal and flammability properties of polypropylene/carbon nanotube nanocomposites, Polymer 45 (2004) 4227–4239.
[15] X. Yan, Q. He, X. Zhang, H. Gu, H. Chen, Q. Wang, L. Sun, S. Wei, Z. Guo, Magnetic polystyrene nanocomposites reinforced with magnetite nanoparticles, Macromol. Mater. Eng. 299 (2014) 485–494.
[16] V. Hadjiev, G. Warren, L. Sun, D. Davis, D. Lagoudas, H.-J. Sue, Raman microscopy of residual strains in carbon nanotube/epoxy composites, Carbon 48 (2010) 1750–1756.
[17] J. Zhu, S. Wei, N. Haldolaarachchige, D.P. Young, Z. Guo, Electromagnetic field shielding polyurethane nanocomposites reinforced with core–shell Fe–silica nanoparticles, J. Phys. Chem. C 115 (2011) 15304–15310.
[18] Z. Guo, S.-E. Lee, H. Kim, S. Park, H. Hahn, A. Karki, D. Young, Fabrication, characterization and microwave properties of polyurethane nanocomposites reinforced with iron oxide and barium titanate nanoparticles, Acta Mater 57 (2009) 267–277.
[19] Z. Guo, S. Park, H.T. Hahn, S. Wei, M. Moldovan, A.B. Karki, D.P. Young, Magnetic and electromagnetic evaluation of the magnetic nanoparticle filled polyurethane nanocomposites, J. Appl. Phys. 101 (2007) 09M511.
[20] J. Njuguna, K. Pielichowski, Polymer nanocomposites for aerospace applications: properties, Adv. Eng. Mater 5 (2003) 769–778.
[21] C. Cooper, R. Young, M. Halsall, Investigation into the deformation of carbon nanotubes and their composites through the use of Raman spectroscopy, Compos. Part A 32 (2001) 401–411.
[22] L. Sun, G. Warren, D. Davis, H.-J. Sue, Nylon toughened epoxy/SWCNT composites, J. Mater. Sci. 46 (2011) 207–214.
[23] G. Gao, T. Cagin, W.A. Goddard III, Energetics, structure, mechanical and vibrational properties of single-walled carbon nanotubes, Nanotechnology 9 (1998) 184.
[24] X. Wang, Q. Li, J. Xie, Z. Jin, J. Wang, Y. Li, K. Jiang, S. Fan, Fabrication of ultralong and electrically uniform single-walled carbon nanotubes on clean substrates, Nano Lett. 9 (2009) 3137–3141.
[25] L. Sun, G. Warren, J. O'reilly, W. Everett, S. Lee, D. Davis, D. Lagoudas, H.-J. Sue, Mechanical properties of surface-functionalized SWCNT/epoxy composites, Carbon 46 (2008) 320–328.
[26] T. Uchida, S. Kumar, Single wall carbon nanotube dispersion and exfoliation in polymers, J. Appl. Polym. Sci. 98 (2005) 985–989.
[27] S. Iijima, Helical microtubules of graphitic carbon, Nature 354 (1991) 56–58.
[28] F. Du, R.C. Scogna, W. Zhou, S. Brand, J.E. Fischer, K.I. Winey, Nanotube networks in polymer nanocomposites: rheology and electrical conductivity, Macromolecules 37 (2004) 9048–9055.
[29] X. Zhang, X. Yan, Q. He, H. Wei, J. Long, J. Guo, H. Gu, J. Yu, J. Liu, D. Ding, L. Sun, S. Wei, Z. Guo, Electrically conductive polypropylene nanocomposites with negative permittivity at low carbon nanotube loading levels, ACS Appl. Mater. Interfaces 7 (2015) 6125–6138.
[30] T. Kashiwagi, E. Grulke, J. Hilding, R. Harris, W. Awad, J. Douglas, Thermal degradation and flammability properties of poly (propylene)/carbon nanotube composites, Macromol. Rapid Commun. 23 (2002) 761–765.
[31] L. Hu, D. Hecht, G. Grüner, Percolation in transparent and conducting carbon nanotube networks, Nano Lett. 4 (2004) 2513–2517.
[32] A.A. Koval'chuk, A.N. Shchegolikhin, V.G. Shevchenko, P.M. Nedorezova, A.N. Klyamkina, A.M. Aladyshev, Synthesis and properties of polypropylene/multiwall carbon nanotube composites, Macromolecules 41 (2008) 3149–3156.
[33] J. Sandler, J. Kirk, I. Kinloch, M. Shaffer, A. Windle, Ultra-low electrical percolation threshold in carbon-nanotube-epoxy composites, Polymer 44 (2003) 5893–5899.
[34] X. Chen, H. Wang, H. Yi, X. Wang, X. Yan, Z. Guo, Anthraquinone on porous carbon nanotubes with improved supercapacitor performance, J. Phys. Chem. C 118 (2014) 8262–8270.
[35] S. Barrau, P. Demont, E. Perez, A. Peigney, C. Laurent, C. Lacabanne, Effect of palmitic acid on the electrical conductivity of carbon nanotubes-epoxy resin composites, Macromolecules 36 (2003) 9678–9680.
[36] Y.J. Kim, T.S. Shin, H.D. Choi, J.H. Kwon, Y.-C. Chung, H.G. Yoon, Electrical conductivity of chemically modified multiwalled carbon nanotube/epoxy composites, Carbon 43 (2005) 23–30.
[37] S. Bose, R.A. Khare, P. Moldenaers, Assessing the strengths and weaknesses of various types of pre-treatments of carbon nanotubes on the properties of polymer/carbon nanotubes composites: a critical review, Polymer 51 (2010) 975–993.
[38] F.H. Gojny, M.H. Wichmann, B. Fiedler, I.A. Kinloch, W. Bauhofer, A.H. Windle, K. Schulte, Evaluation and identification of electrical and thermal conduction mechanisms in carbon nanotube/epoxy composites, Polymer 47 (2006) 2036–2045.
[39] I.W. Hamley, The Physics of Block Copolymers, Oxford University Press, New York, 1998.
[40] J. Zhu, S. Wei, J. Ryu, Z. Guo, Strain-sensing elastomer/carbon nanofiber "metacomposites", J. Phys. Chem. C 115 (2011) 13215–13222.
[41] S. Mecking, L.K. Johnson, L. Wang, M. Brookhart, Mechanistic studies of the palladium-catalyzed copolymerization of ethylene and α-olefins with methyl acrylate, J. Am. Chem. Soc. 120 (1998) 888–899.
[42] M. Lopez-Manchado, M. Arroyo, Effect of the incorporation of pet fibers on the properties of thermoplastic elastomer based on PP/elastomer blends, Polymer 42 (2001) 6557–6563.
[43] K. Premphet, P. Horanont, Phase structure of ternary polypropylene/elastomer/filler composites: effect of elastomer polarity, Polymer 41 (2000) 9283–9290.
[44] C. Li, Y. Zhang, Y. Zhang, C. Zhang, Blends of polycarbonate and ethylene-1-octylene copolymer, Eur. Polym. J. 39 (2003) 305–311.
[45] M.J.O. Guimarães, F. Coutinho, M.C. Rocha, M. Farah, R.E. Bretas, Rheological and morphological properties of high-density polyethylene and poly (ethylene–octene) blends, J. Appl. Polym. Sci. 86 (2002) 2240–2246.
[46] Z. Guo, S. Park, H.T. Hahn, S. Wei, M. Moldovan, A.B. Karki, D.P. Young, Giant magnetoresistance behavior of an iron/carbonized polyurethane nanocomposite, Appl. Phys. Lett. 90 (2007) 053111.
[47] J. Guo, H. Gu, H. Wei, Q. Zhang, N. Haldolaarachchige, Y. Li, D.P. Young, S. Wei, Z. Guo, Magnetite-polypyrrole metacomposites: dielectric properties and magnetoresistance behavior, J. Phys. Chem. C 117 (2013) 10191–10202.
[48] J. Zhu, M. Chen, H. Qu, H. Wei, J. Guo, Z. Luo, N. Haldolaarachchige, D.P. Young, S. Wei, Z. Guo, Positive and negative magnetoresistance phenomena observed in magnetic electrospun polyacrylonitrile-based carbon nanocomposite fibers, J. Mater. Chem. C 2 (2014) 715–722.
[49] H. Gu, X. Zhang, H. Wei, Y. Huang, S. Wei, Z. Guo, An overview of the magnetoresistance phenomenon in molecular systems, Chem. Soc. Rev. 42 (2013) 5907–5943.
[50] H. Gu, J. Guo, H. Wei, S. Guo, J. Liu, Y. Huang, M.A. Khan, X. Wang, D.P. Young, S. Wei, Z. Guo, Strengthened magnetoresistive epoxy nanocomposite papers derived from synergistic nanomagnetite-carbon nanofiber nanohybrids, Adv. Mater 27 (2015) 6277–6282.
[51] M. Wang, W. Wang, T. Liu, W.-D. Zhang, Melt rheological properties of nylon 6/multi-walled carbon nanotube composites, Compos. Sci. Technol. 68 (2008) 2498–2502.
[52] E.E. Rosenbaum, S.G. Hatzikiriakos, C.W. Stewart, Rheological characterization of well-defined tetrafluoroethylene/hexafluoropropylene copolymers, Rheol. Acta 37 (1998) 279–288.
[53] A. Tuteja, P.M. Duxbury, M.E. Mackay, Multifunctional nanocomposites with reduced viscosity, Macromolecules 40 (2007) 9427–9434.
[54] S. Jain, J.G.P. Goossens, G.W.M. Peters, M. van Duin, P.J. Lemstra, Strong decrease in viscosity of nanoparticle-filled polymer melts through selective adsorption, Soft Matter 4 (2008) 1848–1854.
[55] B. Wang, L. Hao, W. Wang, G. Hu, One-step compatibilization of polyamide 6/poly (ethylene-1-octene) blends with maleic anhydride and peroxide, J. Polym. Res. 17 (2010) 821–826.
[56] C.A. Mitchell, J.L. Bahr, S. Arepalli, J.M. Tour, R. Krishnamoorti, Dispersion of functionalized carbon nanotubes in polystyrene, Macromolecules 35 (2002) 8825–8830.
[57] P. Pötschke, M. Abdel-Goad, I. Alig, S. Dudkin, D. Lellinger, Rheological and dielectrical characterization of melt mixed polycarbonate-multiwalled carbon nanotube composites, Polymer 45 (2004) 8863–8870.
[58] J. Zhu, S. Wei, A. Yadav, Z. Guo, Rheological behaviors and electrical conductivity of epoxy resin nanocomposites suspended with in-situ stabilized carbon nanofibers, Polymer 51 (2010) 2643–2651.
[59] W. Xue-Bang, X. Qiao-Ling, S. Shu-Ying, S. Jia-Peng, L. Chang-Song, Z. Zhen-Gang, Low-frequency internal friction study on the structural changes in polymer melts, Chin. Phys. Lett. 25 (2008) 1388.
[60] Y. Gao, Q. Wang, J. Wang, L. Huang, X. Yan, X. Zhang, Q. He, Z. Xing, Z. Guo, Synthesis of highly efficient flame retardant high-density polyethylene nanocomposites with inorgano-layered double hydroxides as nanofiller using solvent mixing method, ACS Appl. Mater. Interfaces 6 (2014) 5094–5104.
[61] M.A.L. Cerrada, R. Benavente, E. Pérez, J. Moniz-Santos, M.R. Ribeiro, Experimental evidence of the glass transition in a metallocene ethylene-1-octene copolymer and its composites with glass fibre, Polymer 42 (2001) 7197–7202.

[62] R. Androsch, Melting and crystallization of poly (ethylene-co-octene) measured by modulated dsc and temperature-resolved X-ray diffraction, Polymer 40 (1999) 2805–2812.
[63] B.C. Giessen, G.E. Gordon, X-ray diffraction: new high-speed technique based on X-ray spectrography, Science 159 (1968) 973–975.
[64] J. Deng, X. Ding, W. Zhang, Y. Peng, J. Wang, X. Long, P. Li, A.S.C. Chan, Magnetic and conducting Fe3O4 cross-linked polyaniline nanoparticles with core–shell structure, Polymer 43 (2002) 2179–2184.
[65] C. Ketloy, B. Jongsomjit, P. Praserthdam, Characteristics and catalytic properties of [t-BuNSiMe 2 Flu] TiMe 2/dMMAO catalyst dispersed on various supports towards ethylene/1-octene copolymerization, Appl. Catal. A 327 (2007) 270–277.
[66] X. Yan, M. Li, J. Long, X. Zhang, H. Wei, Q. He, D. Rutman, D. Cao, S. Wei, G. Chen, G. Zhan, Highly monodisperse sub-microspherical poly (glycidyl methacrylate) nanocomposites with highly stabilized gold nanoparticles, Macromol. Chem. Phys. 215 (2014) 1098–1106.
[67] S. Nazare, B. Kandola, A. Horrocks, Flame-retardant unsaturated polyester resin incorporating nanoclays, Polym. Adv. Technol. 17 (2006) 294–303.
[68] H. Gu, J. Guo, Q. He, S. Tadakamalla, X. Zhang, X. Yan, Y. Huang, H.A. Colorado, S. Wei, Z. Guo, Flame-retardant epoxy resin nanocomposites reinforced with polyaniline-stabilized silica nanoparticles, Ind. Eng. Chem. Res. 52 (2013) 7718–7728.
[69] A. Korobko, N. Bessonova, S. Krasheninnikov, E. Konyukhova, S. Drozd, S. Chvalun, Nanodiamonds as modifier of ethylene-1-octene copolymer structure and properties, Diam. Relat. Mater. 16 (2007) 2141–2144.
[70] A.G. Simanke, G.B. Galland, L. Freitas, J.A.H. da Jornada, R. Quijada, R.S. Mauler, Influence of the comonomer content on the thermal and dynamic mechanical properties of metallocene ethylene/1-octene copolymers, Polymer 40 (1999) 5489–5495.
[71] S. Rabiej, B. Goderis, J. Janicki, V. Mathot, M. Koch, G. Groeninckx, H. Reynaers, J. Gelan, A. Włochowicz, Characterization of the dual crystal population in an isothermally crystallized homogeneous ethylene-1-octene copolymer, Polymer 45 (2004) 8761–8778.
[72] Q. He, T. Yuan, J. Zhu, Z. Luo, N. Haldolaarachchige, L. Sun, A. Khasanov, Y. Li, D.P. Young, S. Wei, Z. Guo, Magnetic high density polyethylene nanocomposites reinforced with in-situ synthesized Fe@ FeO core-shell nanoparticles, Polymer 53 (2012) 3642–3652.
[73] Q. He, T. Yuan, X. Zhang, Z. Luo, N. Haldolaarachchige, L. Sun, D.P. Young, S. Wei, Z. Guo, Magnetically soft and hard polypropylene/cobalt nanocomposites: role of maleic anhydride grafted polypropylene, Macromolecules 46 2357–2368.
[74] A. Alizadeh, L. Richardson, J. Xu, S. McCartney, H. Marand, Y. Cheung, S. Chum, Influence of structural and topological constraints on the crystallization and melting behavior of polymers. 1. Ethylene/1-octene copolymers, Macromolecules 32 (1999) 6221–6235.
[75] J. Gu, N. Li, L. Tian, Z. Lv, Q. Zhang, High thermal conductivity graphite nanoplatelet/UHMWPE nanocomposites, RSC Adv. 5 (2015) 36334–36339.
[76] J. Gu, Q. Zhang, J. Dang, C. Xie, Thermal conductivity epoxy resin composites filled with boron nitride, Polym. Adv. Technol. 2012 (2012) 1025–1028.
[77] J. Gu, Z. Lv, Y. Wu, R. Zhao, L. Tian, Q. Zhang, Enhanced thermal conductivity of SiCp/PS composites by electrospinning-hot press technique, Compos. Part A 79 (2015) 8–13.
[78] J. Gu, C. Liang, J. Dang, W. Dong, Q. Zhang, Ideal dielectric thermally conductive bismaleimide nanocomposites filled with polyhedral oligomeric silsesquioxane functionalized nanosized boron nitride, RSC Adv. 6 (2016) 35809–35814.
[79] P. Kim, L. Shi, A. Majumdar, P. McEuen, Thermal transport measurements of individual multiwalled nanotubes, Phys. Rev. Lett. 87 (2001) 215502.
[80] C. Yu, L. Shi, Z. Yao, D. Li, A. Majumdar, Thermal conductance and thermopower of an individual single-wall carbon nanotube, Nano Lett. 5 (2005) 1842–1846.
[81] A. Moisala, Q. Li, I. Kinloch, A. Windle, Thermal and electrical conductivity of single-and multi-walled carbon nanotube-epoxy composites, Compos. Sci. Technol. 66 (2006) 1285–1288.
[82] C.-W. Nan, G. Liu, Y. Lin, M. Li, Interface effect on thermal conductivity of carbon nanotube composites, Appl. Phys. Lett. 85 (2004) 3549–3551.
[83] A. Babel, D. Li, Y. Xia, S.A. Jenekhe, Electrospun nanofibers of blends of conjugated polymers: morphology, optical properties, and field-effect transistors, Macromolecules 38 (2005) 4705–4711.
[84] E. Yablonovitch, G.D. Cody, Intensity enhancement in textured optical sheets for solar cells, Electron Devices, IEEE Trans. 29 (1982) 300–305.
[85] M. de la Guardia, Biochemical sensors: the state of the art, Microchim. Acta 120 (1995) 243–255.
[86] J. Tauc, Absorption edge and internal electric fields in amorphous semiconductors, Mater. Res. Bull. 5 (1970) 721–729.
[87] A. Hjelm, C.G. Granqvist, J.M. Wills, Electronic structure and optical properties of WO3, LiWO3, NaWO3, and HWO3, Phys. Rev. B 54 (1996) 2436–2445.
[88] N. Serpone, D. Lawless, R. Khairutdinov, Size effects on the photophysical properties of colloidal anatase TiO2 particles: size quantization versus direct transitions in this indirect semiconductor? J. Phys. Chem. 99 (1995) 16646–16654.
[89] M.B. Tzolov, T.-F. Kuo, D.A. Straus, A. Yin, Xu, Carbon Nanotube-silicon heterojunction arrays and infrared photocurrent responses, J. Phys. Chem. C 111 (2007) 5800–5804.
[90] J. Wu, W. Walukiewicz, W. Shan, E. Bourret-Courchesne, J. Ager III, K. Yu, E. Haller, K. Kissell, S.M. Bachilo, R.B. Weisman, Structure-dependent hydrostatic deformation potentials of individual single-walled carbon nanotubes, Phys. Rev. Lett. 93 (2004) 017404.
[91] A.M. Smith, S. Nie, Semiconductor nanocrystals: structure, properties, and band gap engineering, Acc. Chem. Res. 43 (2009) 190–200.
[92] J.D. Fan, Y.M. Malozovsky, Pauli exclusion principle, Int. J. Mod. Phys. B 27 (2013) 1362024.
[93] O. Gülseren, T. Yildirim, S. Ciraci, Ç. Kılıç, Reversible band-gap engineering in carbon nanotubes by radial deformation, Phys. Rev. B 65 (2002) 155410.
[94] L. Yang, M.P. Anantram, J. Han, J.P. Lu, Band-gap change of carbon nanotubes: effect of small uniaxial and torsional strain, Phys. Rev. B 60 (1999) 13874–13878.
[95] Z.H. Ni, T. Yu, Y.H. Lu, Y.Y. Wang, Y.P. Feng, Z.X. Shen, Uniaxial strain on graphene: Raman spectroscopy study and band-gap opening, ACS Nano 2 (2008) 2301–2305.
[96] Y. Li, J. Zhu, S. Wei, J. Ryu, Q. Wang, L. Sun, Z. Guo, Poly(propylene) nanocomposites containing various carbon nanostructures, Macromol. Chem. Phys. 212 (2011) 2429–2438.
[97] G.D. Seidel, D.C. Lagoudas, A micromechanics model for the electrical conductivity of nanotube-polymer nanocomposites, J. Compos. Mater 43 (2009) 917–941.
[98] L. Hu, D.S. Hecht, G. Grüner, Percolation in transparent and conducting carbon nanotube networks, Nano Lett. 4 (2004) 2513–2517.
[99] J. Stejskal, I. Sapurina, M. Trchová, J. Prokeš, I. Krivka, E. Tobolková, Solid-state protonation and electrical conductivity of polyaniline, Macromolecules 31 (1998) 2218–2222.
[100] Z. Guo, K. Shin, A.B. Karki, D.P. Young, R.B. Kaner, H.T. Hahn, Fabrication and characterization of iron oxide nanoparticles filled polypyrrole nanocomposites, J. Nanopart. Res. 11 (2009) 1441–1452.
[101] M. Aggarwal, S. Khan, M. Husain, T. Ming, M. Tsai, T. Perng, Z. Khan, Variable-range hopping in Fe70Pt30 catalyzed multi-walled carbon nanotubes film, Eur. Phys. J. B 60 (2007) 319–324.
[102] B. Hu, Y. Wu, Tuning magnetoresistance between positive and negative values in organic semiconductors, Nat. Mater 6 (2007) 985–991.
[103] T.A. Skotheim, J. Reynolds, Handbook of Conducting Polymers, CRC Press, 2007.
[104] R. Rosenbaum, T. Murphy, E. Palm, S. Hannahs, B. Brandt, Magnetoresistance of insulating amorphous NixSi1-x films exhibiting Mott variable-range hopping laws, Phys. Rev. B 63 (2001) 094426.
[105] S. Bhadra, D. Khastgir, N.K. Singha, J.H. Lee, Progress in preparation, processing and applications of polyaniline, Prog. Polym. Sci. 34 (2009) 783–810.
[106] V.M. Shalaev, Optical negative-index metamaterials, Nat. photonics 1 (2007) 41–48.
[107] Y. Long, Z. Chen, X. Zhang, J. Zhang, Z. Liu, Synthesis and electrical properties of carbon nanotube polyaniline composites, Appl. Phys. Lett. 85 (2004) 1796–1798.
[108] T.-I. Su, C.-R. Wang, S.-T. Lin, R. Rosenbaum, Magnetoresistance of Al70Pd22.5Re7.5 quasicrystals in the variable-range hopping regime, Phys. Rev. B 66 (2002) 054438.
[109] Y. Yosida, I. Oguro, Variable range hopping conduction in bulk samples composed of single-walled carbon nanotubes, J. Appl. Phys. 86 (1999) 999–1003.